



Understanding the effects of material properties and operating conditions on component aging in polymer electrolyte water electrolyzers

Ugljesa Babic^a, Mohamed Tarik^b, Thomas Justus Schmidt^{a,c}, Lorenz Gubler^{a,*}

^a Electrochemistry Laboratory, Paul Scherrer Institut, 5232 Villigen PSI, Switzerland

^b Bioenergy and Catalysis Laboratory, Chemical Processes and Materials Group, Paul Scherrer Institut, 5232 Villigen PSI, Switzerland

^c Laboratory of Physical Chemistry, ETH Zürich, 8093 Zürich, Switzerland

HIGHLIGHTS

- Catalyst layer deformation results in higher proton transport resistance.
- Locally thin areas formed as a result of creep of the catalyst coated membrane.
- Locally thin areas lead to increased gas crossover and fluoride release.
- Start-stop operation: more pronounced Ir-dissolution, but kinetic losses are unaffected.

ARTICLE INFO

Keywords:

Water electrolysis degradation
Water electrolyzer diagnostics
Catalyst layer aging
Polymer electrolyte membrane degradation

ABSTRACT

If polymer electrolyte water electrolysis (PEWE) is to penetrate the energy market in the context of power-to-x, challenges related to component durability need to be understood and addressed. In this study, PEWE component degradation mechanisms are induced by combining catalyst-coated membranes (CCMs) with specific cell materials and operating conditions. The effect of the cell compression on the catalyst layer performance is investigated using cell assemblies with porous transport layers (PTLs) having different material properties. Rigid PTL-surface features result in local variation in anode catalyst layer (CL) porosity, and increased CL proton transport resistance. The creep of the CCM leads to the formation of thin sections and an increase in the content of H₂ in the O₂ product gas, causing in turn higher fluoride release rate from the ionomer/membrane. In addition, PEWE cells are subjected to a start-stop protocol to promote catalyst degradation through the formation of active, but unstable iridium hydroxo species. An increasing trend of catalyst dissolution is observed in the case of CCM samples that were operated at higher potential.

1. Introduction

Water electrolysis could become a key technology for the conversion of electricity from fluctuating renewable sources to hydrogen and a backbone of future energy systems. Produced H₂ can be later re-electrified or utilized in the mobility or industry sectors. Furthermore, water electrolysis can serve as a coupling element between different sectors (electricity, heating, mobility) in the framework of power-to-liquid or power-to-gas concepts [1–3]. Polymer electrolyte water electrolysis (PEWE) stands out from the other water electrolysis technologies in this context, such as the traditional and established alkaline water electrolysis, since the thin polymer membrane (<200 μm) allows high current density (*i*) operation and large differential pressures (>50 bar).

The main challenges for PEWE technology are high costs and durability of its components [4,5]. Overall, stack components contribute about 60% to the total investment costs of a modern PEWE system [6]. The acidic environment and high electrochemical potentials restrict the choice of anode catalyst (Ir) and porous transport layer (PTL) material (Ti). On the other hand, high PEWE stack voltage efficiency is necessary to reduce the end-cost of the produced H₂ since the operational costs are dominated by the price of electricity [7]. The efforts in material innovation and component optimization towards less expensive and more efficient PEWE stacks must not consequently affect the durability, considering the projected lifetime of PEWE systems of >80'000 h [8]. Furthermore, the development of standardized accelerated stress tests (ASTs) for PEWE components is necessary to increase the throughput of material and guide the innovation efforts. In spite of efforts in the

* Corresponding author.

E-mail address: lorenz.gubler@psi.ch (L. Gubler).

<https://doi.org/10.1016/j.jpowsour.2020.227778>

Received 9 September 2019; Received in revised form 9 January 2020; Accepted 20 January 2020

Available online 14 February 2020

0378-7753/© 2020 Elsevier B.V. All rights reserved.

Glossary

AST	Accelerated stress test
CCM	Catalyst coated membrane
CL	Catalyst layer
CV	Cyclic voltammetry
EDX	energy dispersive X-ray spectroscopy
EIS	Electrochemical impedance spectroscopy
FRR	Fluoride release rate
GDL	Gas diffusion layer
HFR	High frequency resistance
IC	Ion chromatography
ICP-MS	Inductively coupled plasma mass spectrometry
OCV	Open circuit voltage
OER	Oxygen evolution reaction

PEWE	Polymer electrolyte water electrolysis
PTL	Porous transport layer
SEM	Scanning electron microscope
E_{cell}	Cell voltage
$E_{\text{rev}}^{\text{p,T}}$	Reversible cell voltage
$E_{\text{iR-free}}$	iR free cell voltage
i	Current density
$R_{\text{CL}}^{\text{H}^+}$	Proton transport resistance in the catalyst layer
R_{PEM}	Membrane ionic resistance
R_{el}	Cell electronic resistance
η_{ohm}	Ohmic overpotential
η_{kin}	Kinetic overpotential
η_{mtx}	Mass transport overpotential

electrolyzer community, there are currently no ASTs specified for PEWE. Understanding the main stressors and degradation mechanisms is key towards formulating ASTs that trigger specific types of degradation in order to tailor the next generation of PEWE materials and components. In this work, we focus on the aspects of PEWE component aging, which have not been addressed extensively in the literature, i.e., the mechanical degradation of the catalyst layer (CL) and the membrane, and the dissolution of the catalyst material. The experimental findings in this work provide a direction to diagnose PEWE component aging and a stepping-stone towards defining ASTs for the PEWE community.

1.1. Mechanically induced degradation

The effect of the mechanical deformation of the catalyst-coated membrane (CCM) on the overpotential is often not addressed in the literature, but it could be a limiting step for the implementation of thin membranes in PEWE. Since the overpotential at high current densities is dominated by the ohmic resistance of the polymer electrolyte, the development of electrolyzers with high voltage efficiency could be bottlenecked by the mechanical creeping and possible shorting of the CCM. So far, the mechanical compression of the CCM has been investigated in the context of optimizing the contact resistance between the cell components [9]. Rakousky et al. have observed the mechanical creep of the membrane under constant mechanical stress that resulted in lower ohmic resistance [10]. Recently, dependence of the interfacial contact area between the PTL and the CCM on the membrane deformation was studied using X-ray tomography [11]. Besides the reduction in the ohmic resistance with higher clamping pressures, Frensch et al. have reported larger exchange current densities on the account of higher electrochemically active surface area due to the increased number of contact points between the porous transport layer (PTL) and the CL at higher cell compression levels [12]. In this study, we investigate the combined effects of cell compression and PTL surface properties on the CL performance by using PTLs with different material properties.

Surface properties of PEWE PTLs have been shown to affect the morphology of the catalyst layer, and thereby the proton transport resistance in its ionomer phase ($R_{\text{CL}}^{\text{H}^+}$) [13]. The impact of the mechanical deformation on the catalyst layer transport properties was quantified by measuring the impedance response of the PEWE anodes in the H_2/N_2 regime. The effect of the PTL pore size and type on the membrane deformation was observed post-test on samples using scanning electron microscopy (SEM). Local membrane thinning effects on the gas crossover are quantified by measuring H_2 crossover during the experiments with different PTLs. Since the gas crossover proved to be significantly higher in the case of mechanically impaired membranes, fluoride release rate (FRR) measurements were employed to correlate the mechanical deformation of the membrane and the chemical degradation of the

polymer. The polarization curve breakdown was done according to the Tafel model [14–16] to pinpoint the effect of the ionic contamination on the overpotentials.

1.2. Catalyst dissolution

Kinetic losses related to the oxygen evolution reaction (OER) contribute a large fraction to the overpotential in PEWE [13,15,17], and can be reduced by developing more active catalyst [18–21] with higher surface area [22–24], using more catalyst material during the CCM preparation [17,25], and optimizing the CL/PTL interface for better catalyst utilization [17,26,27]. It is difficult to fully substitute Ir in acidic PEWE environment due to stability and activity constraints [28–30]. Additionally, one of the long-term goals of the PEWE community is to reduce the Ir-loading to facilitate large-scale penetration of the technology [4]. Considering the projected lifetime of PEWE [8], it is also important to maintain the stability and catalytic activity of the material under dynamic operating conditions. Kasian et al. have shown that the dissolution of Ir can follow different pathways depending on the anode potential [30]. Higher anode potentials (and the resulting current densities) were correlated with more pronounced dissolution rates of Ir [30]. Furthermore, more Ir was detected after low potential steps [31]. Recently Weiß et al. have shown that a parasitic ohmic resistance might occur at the interface between the PTL and the hydrous Ir oxide, resulting in additional voltage losses [32].

In this study, PEWE cells with Ir-based anodes were operated in start-stop mode for 300 h with different on-state potentials. Ir-dissolution was quantified using inductively coupled plasma mass spectrometry (ICP-MS) on the anode water samples. CCM cross-sections were analyzed using energy dispersive X-ray spectroscopy (EDX) post-test to detect Ir that might have precipitated in the ionomer [33]. The cell voltage was varied to investigate the dependence of the Ir dissolution on the anode potential (on-states), while the open circuit voltage (OCV) (off-states) were introduced to promote the formation of surface-hydroxo-Ir species [22]. Hydroxo Ir-species have been detected and correlated with higher catalyst activity but lower stability [23,32,34]. PEWE cells were characterized using electrochemical impedance spectroscopy (EIS) and cyclic voltammetry (CV) to study the effects of different operating conditions on the transport and kinetic properties of the anode catalyst layer.

2. Experimental

2.1. PEWE cell and test-bench

Experiments were conducted in an in-house developed test-bench described elsewhere [13]. Polarization curves, EIS spectra and the CVs

were collected using a SP-150 potentiostat paired with a VMP3B-80 booster from BioLogic. CL proton transport properties were extracted from the EIS spectra collected in the H_2/N_2 regime according to the methodology described in detail in Ref. [35]. The N_2 stream was injected into the anode cell compartment at 400 NmL min^{-1} , and the humidified H_2 was circulated in the cathode cell compartment at 500 NmL min^{-1} . CCMs were immersed in ultrapure (18 MOhm) water overnight before assembly. PEWE cells with a 25 cm^2 active area and a parallel flow field design were conditioned for 12 h before the measurements by cycling the current density i between 1 and 2 A cm^{-2} at 60°C . Initial polarization curves, EIS (in regular and H_2/N_2 regime) and CVs were recorded after conditioning for each cell to serve as a baseline. After the experiment, the cells were analyzed in the same manner.

2.2. Analytical techniques

CCM cut-outs were immersed in liquid N_2 up to 1 min, and fractured to preserve the cross-sectional features, and prepared for the SEM analysis (Zeiss Supra VP55) by sputter-coating the fracture surface with a 7–10 nm thick Cr layer. CCM thickness measurements were taken approximately every $40 \mu\text{m}$ along the CCM cross-section to quantify the extent of the deformation. Elemental mapping using EDX was used to detect the dissolved Ir species in the membrane. Acceleration voltage was 20 kV, with a working distance of 11 mm and an aperture of $60 \mu\text{m}$. Whole cross-sections were scanned, and regions of $12 \times 5 \mu\text{m}$ were analyzed with respect to the Ir distribution in the vicinity of the anode catalyst layer.

Water was collected periodically from the cathodic cell compartment for analysis of traces of F-ions using ion-chromatography (Metrohm 882 Compact), with a detection limit of 100 ppm. Water from the anode test-bench compartment was analyzed for traces of Ir using ICP-MS (Agilent 7700x). These analytical methods enable us to detect dissolved Ir that might be present in the feed water or had precipitated in the membrane. A portion of the dissolved Ir could galvanically replace less noble metals in test bench components (fittings and separator), and is could not be quantified in this analysis. The ICP-MS system was optimized by using tuning solution of 1 ng mL^{-1} Li, Co, Y, Ce, Tl and Ir in order to achieve high sensitivity and low oxidation rate (CeO/Ce below 1.5%). Following parameters were set: power 1350 W, sampling depth 10 mm, carrier gas Ar 0.93 L min^{-1} . The two Ir isotopes were measured at m/z 191 and 193 with an integration time of 0.1 s each. The analysis was performed in pulsed mode and due to the low interferences at both m/z 's no-gas was used for the collision cell. Sensitivity of $78.88 \text{ cps (pg mL}^{-1})^{-1}$ and $135.48 \text{ cps (pg/mL}^{-1})^{-1}$ and LOD (limit of detection) of 0.20 pg mL^{-1} and 0.11 pg mL^{-1} were obtained for ^{191}Ir and ^{193}Ir , respectively. The quantification was carried out by using external calibration and Ir commercial standard solution (from Inorganic Ventures) with concentrations of 0, 0.05, 0.5 and 5 ppb (ng mL^{-1}).

2.3. Experimental conditions

The PEWE cells were assembled using commercial CCMs with Ir-based anode and Pt-based cathode CLs. Detailed cell configuration, the CCM/PTL materials and the experimental conditions are shown in

Table 1

List of components and operating conditions of PEWE cells, assembled to promote mechanical and catalyst layer degradation and the dissolution of Ir. Cell 1 was used as a reference cell. Cell 2 was assembled with a PTL in the cathode cell compartment to mechanically stress the CCM. Cells 3 and 4 were operated in the start stop regime to promote catalyst dissolution.

Reference	CCM	PTL _a	PTL _c	Operating conditions	T ($^\circ\text{C}$)
Cell 1 (reference)	N115 – based, commercial	GKN T10	Spectracarb 2050A (1.5 mm)	2 A cm^{-2} steady state, 300 h	60°C
Cell 2	N115 – based, commercial	GKN T10	GKN T10	2 A cm^{-2} steady state, 300 h	60°C
Cell 3	N117 – based, commercial	GKN T10	Spectracarb 2050A (1.5 mm)	OCV – 1.8 V, 60 s intervals for 300 h	60°C
Cell 4	N117 – based, commercial	GKN T10	Spectracarb 2050A (1.5 mm)	OCV – 2.2 V, 60 s intervals for 300 h	60°C

Table 1. Normally, the cell was assembled by sandwiching the CCM between the anodic Ti-sintered PTL (GKN T10, 1 mm) and the gas diffusion layer (GDL) in the cathode compartment (cell 1). The cathode GDL deforms under the compression from the cell assembly, since it is compressible under the nominal assembly clamping pressures (2–3 MPa). The effect of the mechanical stress of the CCM was promoted by assembling a cell with the sintered-Ti PTLs in both cell compartments (cell 2). The CCM is compressed under the particles of the sintered-PTL in this rigid setup, and creeps into the voids of the PTL under the clamping pressure (Fig. 1a). The cells were operated for 300 h at a steady-state current density of $i = 2 \text{ A cm}^{-2}$ and a temperature of 60°C . Ion-exchange resin (Lewatit MonoPlus S 108 H and MP 62) was implemented in the anode water recirculation loop to eliminate the effect of the ionic contamination in experiments with cells 1 and 2.

The effect of intermittent operating conditions on the Ir-dissolution was induced by operating the electrolyzer potentiostatically in start-stop (i.e., between the operation cell voltage and OCV) mode in 60 s intervals for 300 h at 60°C . The on-state cell voltage was varied between 1.8 and 2.2 V (cell 3 and cell 4, respectively). Ion-exchange resin was not present in the experiments with cells 3 and 4, in order to quantify all Ir-species dissolved in the anodic water. CCMs were treated with 0.5 M H_2SO_4 post-test to eliminate the effect of cationic contamination on the cell performance.

2.4. Cell voltage breakdown

The polarization curve breakdown was done according to the Tafel analysis [14–16]. The cell voltage (E_{cell}) is composed of the reversible cell voltage ($E_{\text{rev}}^{\text{p,T}}$) and the overpotential related to the kinetic (η_{kin}), ohmic (η_{ohm}) and mass-transport losses (η_{mtx}):

$$E_{\text{cell}} = E_{\text{rev}}^{\text{p,T}} + \eta_{\text{kin}} + \eta_{\text{ohm}} + \eta_{\text{mtx}} = E_{\text{rev}}^{\text{p,T}} + \eta_{\text{kin}} + i \cdot (R_{\text{PEM}} + R_{\text{el}}) + i \cdot (R_{\text{CLa}}^{\text{H}^+} + R_{\text{CLc}}^{\text{H}^+}) + \eta_{\text{rest}}$$

The high frequency resistance (HFR), a sum of the cell electronic resistance (R_{el}) and the membrane ionic resistance (R_{PEM}) was measured at 10 kHz during the galvanostatic steps of the polarization curve and the resulting η_{ohm} was subtracted from E_{cell} to yield the iR-free cell voltage ($E_{\text{iR-free}}$). The Tafel slope b is fitted in the low- i region (0.01 – 0.1 A cm^{-2}) where no mass-transport losses are expected. Subtraction of $E_{\text{rev}}^{\text{p,T}}$, given by the Nernst equation, yields the activation overpotential η_{kin} . Kinetic losses stem from the sluggish anodic reaction [14,17], and the contribution of the kinetically fast hydrogen electrode can be neglected from the analysis. η_{mtx} is partially related to the proton transport resistance in the catalyst layers ($R_{\text{CLa}}^{\text{H}^+}$, $R_{\text{CLc}}^{\text{H}^+}$) [13,26]. Since the cathode reaction is fast, the $R_{\text{CLc}}^{\text{H}^+}$ is assumed to be negligible [26]. The contribution of $R_{\text{CLa}}^{\text{H}^+}$ to η_{mtx} was determined from the EIS spectra collected in the H_2/N_2 regime [13,35].

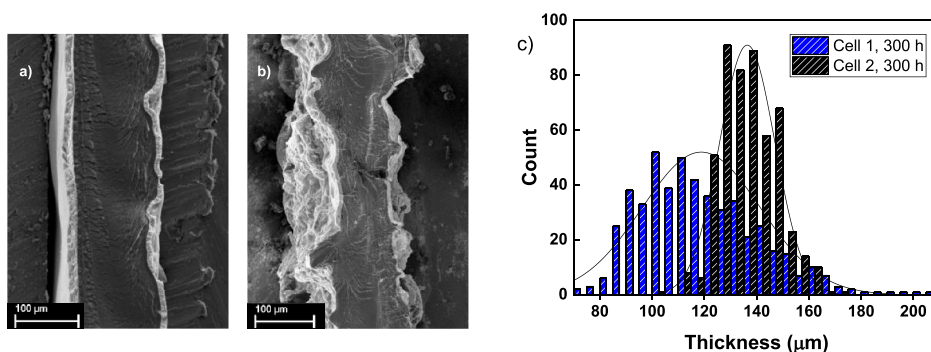


Fig. 1. SEM images of a post-test CCM cross-section from cell 1 (a) and cell 2 (b), and (c) histogram with the distribution of CCM thickness obtained from the SEM scans of CCM cross-sections with the measurements taken 40 μm apart (see section 5.2, “Analytical techniques”).

3. Results and discussion

3.1. Mechanically-induced degradation

3.1.1. Physical characterization

Cell 2 was assembled to promote the mechanical stress on the CCM. The CCM is compressed by the sintered PTL particles, and creeps into the PTL voids under the cell clamping force (Fig. 1b). Deviation from the mean thickness (nominal thickness of the dry N115 membrane is $\sim 125 \mu\text{m}$) is more pronounced in the case of the CCM cross-section from cell 2 (Fig. 1c). Furthermore, the histogram indicates a significant local thinning of the CCM in the case of cell 2, with thickness values below $100 \mu\text{m}$ occurring relatively frequently. The cross-section of the CCM from the reference cell 1 did not exhibit extreme local thinning. Likewise, the morphology of catalyst layers was preserved in the case of cell 1 (Fig. 1a), whereas the catalyst layers of the CCM from cell 2 exhibit frequent cracks and fissures (Fig. 1b).

3.1.2. Cell voltage breakdown

Cell 2 exhibited a higher degradation rate ($\sim 2.9 \text{ mV h}^{-1}$) in the first 40 h, which leveled off to a $\sim 0.1 \text{ mV h}^{-1}$ from 100 to 300 h (Fig. 2a). Cell 1 on the other hand showed a steady degradation rate of $\sim 0.03 \text{ mV h}^{-1}$. Polarization curves measured at the beginning and the end of the experiment (Fig. 2b) show that the cell 2 configuration with two PTLs affected the losses more than those of cell 1 with a GDL in the cathode cell compartment. Overall, the overpotential of the cell 2 had increased by 80–100 mV in the i range of $1\text{--}3 \text{ A cm}^{-2}$ over 300 h. At the first glance, there is no significant difference in the polarization curves of reference cell 1.

E_{cell} was iR -corrected to obtain $E_{iR\text{-free}}$ (Fig. 2c), which contains only the kinetic and mass-transport contribution to the overpotential. $E_{iR\text{-free}}$ increased for both cells 1 and 2, with more pronounced non-ohmic losses in the case of cell 2. Full breakdown of losses at 1, 2 and 3 A cm^{-2} (Fig. 3) shows that all overpotentials ($\eta_{\text{ohm}}, \eta_{\text{kin}}, \eta_{\text{mtx}}$) had increased in the case of the cell 2. Decrease of η_{ohm} was offset by an increase of η_{mtx} for cell 1,

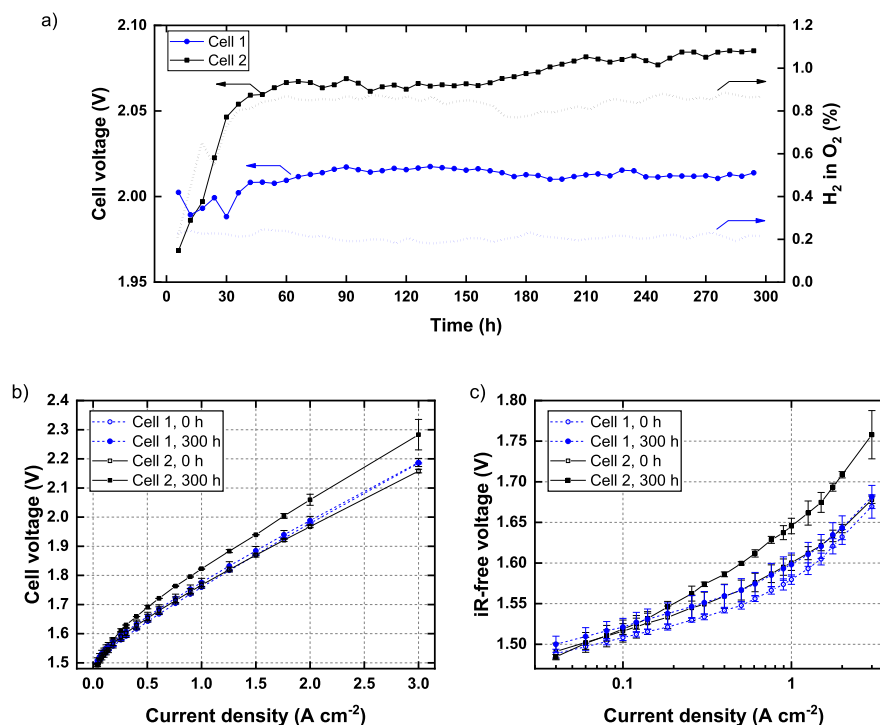


Fig. 2. a) Cell voltage and H_2 content in the O_2 stream during the 300 h steady state experiments with a mechanically stressed cell 2 and a reference cell 1 with a GDL in the cathode cell compartment at 60°C and 2 A cm^{-2} . b) Polarization curves and c) iR -free cell voltage at the beginning and the end of experiments with cells 1 and 2, measured at 60°C and 1 bar_a .

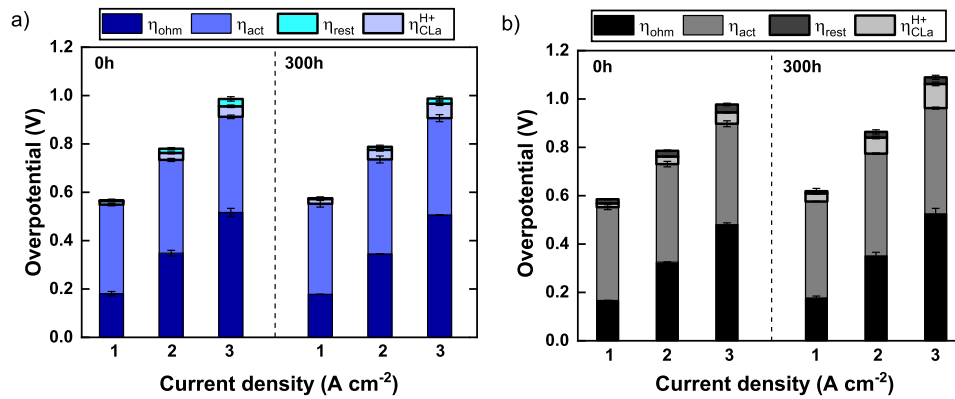


Fig. 3. Cell voltage breakdown into ohmic, kinetic and mass transport overpotential (corrected for the contribution of the anode catalyst layer, $\eta_{CLa}^{H^+}$) at 1, 2 and 3 A cm^{-2} at the beginning and the end of a 300 h steady state experiment at 60 °C and 2 A cm^{-2} with a mechanically stressed cell 2 (b) with two PTLs and reference cell 1 (a) with a GDL in the cathode cell compartment.

which resulted in similar polarization curves before and after the experiment. Rakousky et al. have identified CCM creep as one of the phenomena affecting the contact resistance, which can explain lower η_{ohm} in the case of the small degree of CCM deformation induced by the cell 1 configuration (Fig. 1a) [10]. In the case of cell 2, the deformation of the CCM was more pronounced, leading to pronounced creep of the CCM into the PTL pores ($d_{50}^{pore} \approx 70 \mu\text{m}$ [15]), and fissures in the CL structure, which could adversely affect the contact resistance. η_{kin} was found to be lower for cell 1 at the beginning of experiment. Although only the cathode PTL was changed to a GDL, its compressible properties result in a uniform contact between the PTL/GDL and the catalyst layers [12] (Fig. 1). The average oxidation/reduction current in the CV (0.8–1.2 V) is higher for cell 1 as well (Fig. 4a), implying a better utilization of the catalyst [17].

Among all overpotentials, the largest relative change for cells 1 and 2 over 300 h was observed for η_{mtx} . To determine if the nature of the additional η_{mtx} was related to the proton transport in the anode catalyst layer, the EIS response of cells 1 and 2 in the H_2/N_2 regime (Fig. S1) was analyzed. The steps taken to obtain $R_{CLa}^{H^+}$ are given in detail elsewhere [35]. In our previous work we have found that the PTL surface morphology (pore and particle size) determines the level of CCM deformation, and consequently the extent of losses associated with proton transport in the anode catalyst layer [13]. The $R_{CLa}^{H^+}$ for both cells is approximately the same at the beginning of experiment (10.5 ± 1.5 and $10.7 \pm 0.4 \text{ m}\Omega \text{ cm}^2$ for the cell 1 and cell 2, respectively), making up 40% of the calculated η_{mtx} . In the case of cell 2, $R_{CLa}^{H^+}$ had increased to

$29.6 \pm 2.3 \text{ m}\Omega \text{ cm}^2$ after 300 h (Fig. 5), accounting for the increase of measured η_{mtx} . On the other hand, $R_{CLa}^{H^+}$ of cell 1 increased to $16.2 \pm 2.2 \text{ m}\Omega \text{ cm}^2$ after 300 h, significantly less than for cell 2 configuration.

The deformation of the catalyst layer leads to breaks in the proton

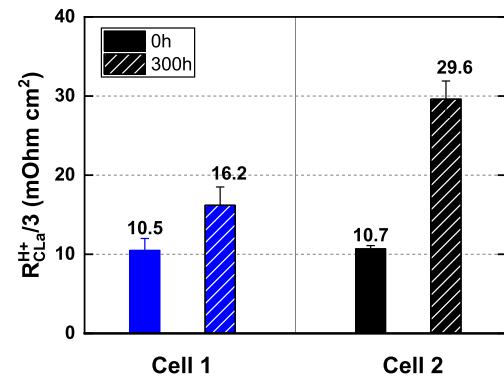


Fig. 5. Proton transport resistance measured in the H_2/N_2 regime (60 °C) at the beginning and the end of a 300 h steady-state experiment at 2 A cm^{-2} and 60 °C with a mechanically stressed cell 2 with two PTLs and a reference cell 1 with a GDL in the cathode cell compartment.

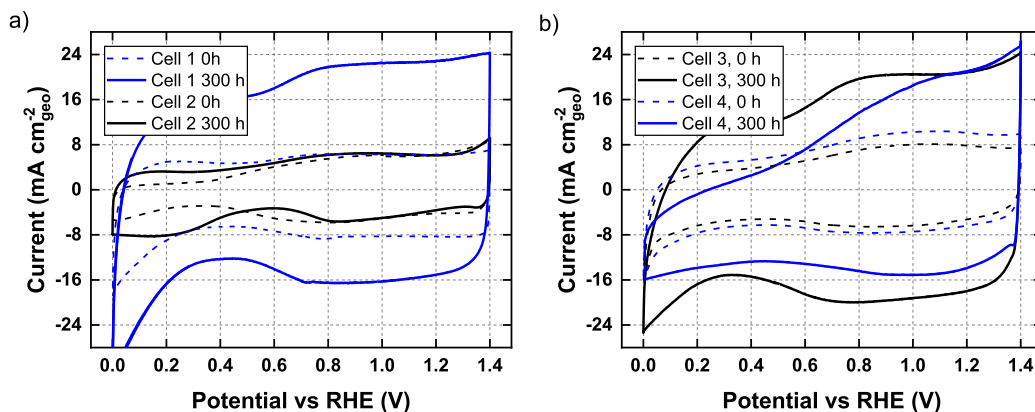


Fig. 4. Cyclic voltammograms of a) reference cell 1 and the mechanically stressed cell 2; b) cell 3 (OCV – 1.8 V) and cell 4 (OCV – 2.2 V), measured under H_2/N_2 at 60 °C at 50 mV/s sweep rate and cathode as a reference electrode.

transport network and increases the diffusion distance for the reactant to reach the active sites under the PTL particles [13,27]. This effect is more pronounced in the case of cell 2, where the mechanical deformation of the CCM is promoted by the incompressible PTL with large pores in both cell compartments (Fig. 1a). After subtraction of the $R_{\text{CLa}}^{\text{H}+}$ contribution, the η_{rest} was similar for both cells before and after the experiment, amounting to 45 ± 6 mV and 33 ± 11 mV at 3 A cm^{-2} for cell 2 and cell 1, respectively (Fig. 3). This means that the unaccounted part of η_{mtx} does not significantly change during the experiment in both cells. As such, it might not be related to proton transport, and could have an origin in other cell components [15,36].

3.1.3. Mechanical-chemical degradation coupling via gas crossover

The concentration of H_2 in the O_2 outlet for cell 2 increased from $\sim 0.2\%$ to $\sim 1.0\%$ at the same time when E_{cell} shows the highest degradation rate. CCM post-test thickness distribution in Fig. 1c indicates significantly more local thin areas in the case of cell 2, which could promote gas crossover. On the other hand, excessive compaction of the catalyst layers might induce gas supersaturation effects described by Trinke et al. [37], and increased gas crossover. Higher gas crossover can induce a higher rate of radical formation and accelerated decomposition of the membrane material [38–40]. Chemical membrane degradation can be diagnosed by analyzing the effluent cathodic water (electro-osmotically dragged water) for fluoride ions emitted from the CCM ionomer [41]. Electroosmotically dragged water was periodically collected from the cathode test-stand compartment and analyzed using ion-chromatography. The FRR was constant over 300 h in the case of cell 2 ($\sim 0.2 \mu\text{g}/(\text{cm}^2\cdot\text{h})$) (Fig. 6). The FRR for cell 1 had similar values as the FRR of cell 2 at the beginning of experiment, but then leveled off to $\sim 0.09 \mu\text{g}/(\text{cm}^2\cdot\text{h})$ after 100 h and stayed constant until the end of experiment. Similar conditioning effects were observed for Nafion membranes in fuel cell applications [42]. High initial FRR of cell 1 could be a consequence of the membrane run-in. Since the CCM material and the operating conditions were the same for the two cell configurations, a difference in FRR for the two cells would stem from different gas crossover rates. The presence of FRR-accelerating transition metals (Fe, Cu, Ni) ions is not expected to contribute to the results, since the test-benches contained an ion-exchange resin in the anode water loop to purify the inlet water from test-bench contaminants.

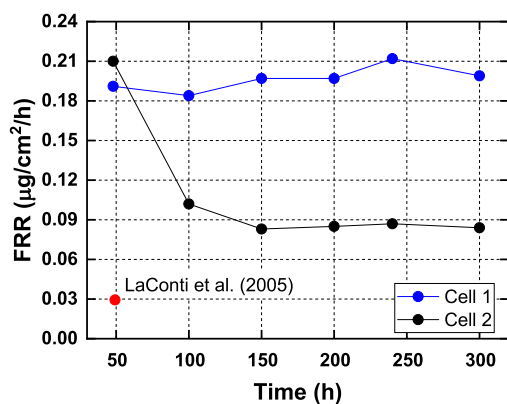


Fig. 6. Fluoride release rate (FRR) during the 300 h constant current experiments (2 A cm^{-2} , 60°C) with cells 1 and 2. The red marker indicates an FRR value found in literature for PFSA membranes at 60°C . (For interpretation of the references to color in this figure legend, the reader is referred to the Web version of this article).

3.2. Start-stop induced degradation

3.2.1. Effect on the cell voltage

Cells 3 and 4 have been assembled using the same components but operated at different conditions with the goal to promote catalyst dissolution. It has been shown that the Ir-based catalysts are reduced at low anodic potentials to form surface hydroxide layers, associated with high electrochemical activity. Cells 3 and 4 have been operated in start-stop mode to trigger the reduction of the Ir-catalyst surface at low potential and via the increased presence of hydrogen (permeated from the cathode cell compartment) in the anode catalyst layer [31]. This procedure resulted in a lower electrolyzer current at the beginning of the experiment (Fig. 7a, 240 s on-state duration for better visualization, current normalized to the average current from the on-state cycle) for both the cells 3 and 4. This is in line with the previous findings regarding the effect Ir-catalyst surface composition on the electrochemical activity, albeit in a half-cell configuration [23,29,31,43]. It is worthwhile mentioning that the measured cell housing and inlet water temperature did not increase between the cycles to cause larger i after the OCV state. Moreover, the effective temperature of the CCM is expected to decrease over the duration of the OCV period, which would in turn result in lower current density upon switching back to the on-state. Only a change in the catalytic activity during the potential cycling would explain higher current density. A similar effect was observed in an operating PEWE cell by Lettenmeier et al. during the start-stop procedure [33].

The current density i plateaued for cells 3 and 4 and started to decay until the end of experiment (Fig. 7b, normalized to the value at the beginning of test). Observed high degradation rates are predominantly a result of the reversible degradation from metallic system components of the anode water recirculation loop, since the ion exchange resin was removed to avoid scavenging of dissolved Ir-species. The difference in degradation rates from the operating conditions is therefore difficult to pinpoint. The CCMs were reprotonated *ex situ* post-test using $0.5 \text{ M H}_2\text{SO}_4$, reassembled and characterized again in the cell. Polarization curves of the ionically contaminated and reprotonated CCMs after 300 h are displayed in Fig. S2 of the supplementary material. The effect of the cationic contamination on the overpotential is not further discussed in this work and is the subject of an independent study. To our knowledge, a correlation between the presence of contaminating cations and catalyst dissolution has not been reported in the literature and cannot be found in this study, and their effect on the Ir-dissolution rate was discarded from the discussion.

Both cells 3 and 4 (reprotonated) perform better after 300 h compared to the beginning of experiment, with cell 3 outperforming cell 4 on the account of lower ohmic losses (Fig. S3). Although no discoloration of the Ti-PTL from cell 4 was observed to indicate a higher degree of Ti-surface passivation [44], a higher cell potential in the case of cell 4 might be responsible for the TiO_2 formation and higher HFR. Additional parasitic ohmic losses have been shown to occur upon the formation of the hydrous Ir-oxide surface layer during dynamic operating conditions [32]. Observed changes in the anodic CVs for cells 3 and 4 (Fig. 8) show a more pronounced hydrogen adsorption-desorption region, which is characteristic for metallic Ir [45]. These features are present in the CV of the reference cell 1 (300 h) as well, indicating that the start-stop operation was not responsible for the development of the hydrogen adsorption/desorption region.

3.2.2. Dissolution and precipitation of Ir

Post-test CCM analysis using an SEM with EDX add-on was conducted with the goal of tracking the catalyst species that might had dissolved and precipitated in the membrane. In a previous study the presence of metallic Ir particles in the membrane after prolonged operation of the electrolyzer at high current densities have been observed in the vicinity of the anode CL [33]. Ir was present in the form of dispersed nanoparticles and a diffuse layer in the catalyst/membrane interface. Dispersed Ir nanoparticles were not detected in the SEM

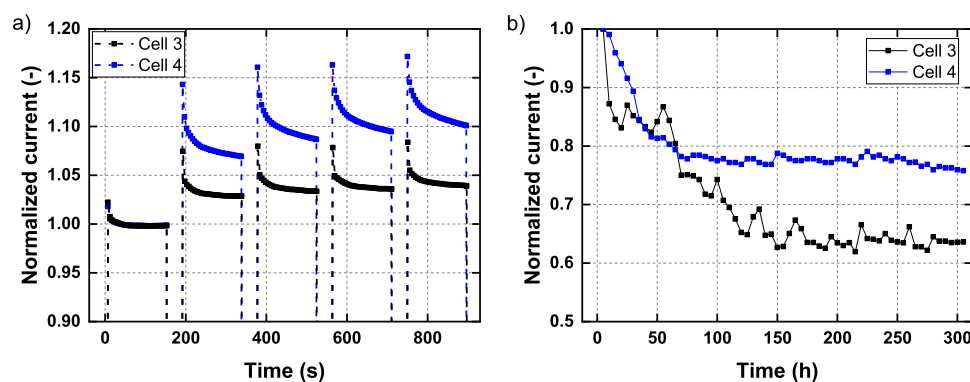


Fig. 7. Current, normalized to the average of a first on-step with cell 3 (OCV-1.8 V, 60 s intervals) and 4 (OCV-2.2 V, 60 s intervals), at a) the beginning and b) during the of 300 h start-stop experiments.

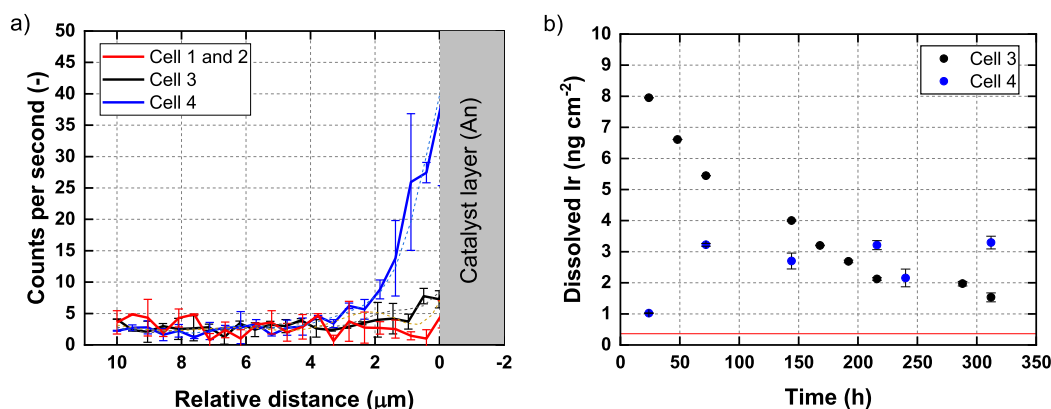


Fig. 8. a) Signal of Ir near the anode catalyst/membrane interface (0 on the x-axis) for cells 1–4, obtained by EDX mapping. Acceleration voltage was 20 kV, with a working distance of 11 mm and an aperture of 60 μm, 2 h per scan. (signal for 1 and 2 combined in red). Whole cross-sections were scanned, and regions of $12 \times 5 \mu\text{m}$ were analyzed to plot the distribution of Ir in the vicinity of the anode catalyst layer. b) Dissolved Ir in the anode water loop (detected using ICP-MS) for cells 3 (OCV-1.8 V, 60 s intervals) and 4 (OCV-2.2 V, 60 s intervals). The red line indicates a blank sample, collected from the circulating test-bench water before the experiment. (For interpretation of the references to color in this figure legend, the reader is referred to the Web version of this article).

cross-sections of CCMs used in this study. Cross-sections contained larger catalyst agglomerates ranging from 2 to 10 μm in the case of some cryo-fractured samples, which were an artifact of the sample preparation. Such samples were excluded from the EDX measurements. On the other hand, a diffuse bright layer near the anode catalyst/membrane interface was detected in the case of cells 3 and 4. A similar region of dissolved Ir (~5 μm in thickness) was observed in the case of Ir-black anodes after 750 h of operation at high i (4 A cm^{-2}) by Lettenmeier et al. [33]. In the case of cells 3 and 4, this region is somewhat smaller (1–3 μm). The difference might stem from the different anode catalyst composition, operating conditions and testing duration. The Ir signal in CCMs from cells 1 and 2 is negligible, indicating that the steady state potential did not lead to degradation of the catalyst and formation of the species which precipitate in the membrane. The formation of the reduced, hydroxo Ir surface species appears beneficial for the activity of the catalyst (Fig. 7a). Higher rates of Ir dissolution have been measured in *in situ* dissolution measurements during the potential hold after OCV conditions [31]. In this study, the Ir-signal was strongest in the CCM cross-section of cell 4, where the potential was cycled between 2.2 V and OCV. This signal is above the background noise level up to 3 μm from the catalyst/membrane interface (Fig. 8a). ICP-MS measurements of the anodic water samples (Fig. 8b) show that significantly more Ir was present in the recirculation loop in the case of cell 3 during the first 150 h. Overall, the dissolution rate followed a decreasing trend for cell 3.

Although initially lower, the Ir dissolution rate increased slightly during the experiment with cell 4. It is important to note that the decreasing level of Ir in the anodic water of cell 3 could be the result of galvanic replacement of Ir-ions with less noble metals of the anodic water loop system components. Another fraction of the dissolved Ir is likely to be exchanged with protons from the CCM ionomer. Finally, higher initial concentration of Ir in the anodic water (cell 3) might not stem from the operating conditions and could be a result of CCM preparation. Nevertheless, the presented findings are in line with the literature on more intense dissolution of Ir-based catalyst at higher anodic potentials [30, 31]. More dissolved Ir from the anode CL, together with differences in CVs of cells 3 and 4 point at the possible effect of start-stop operating conditions on η_{kin} . This is interestingly not the case, as η_{kin} was in the range of error for cells 3 and 4. The results point to the fact that Ir dissolution most likely does not present a critical issue with current commercial grade CCMs with Ir loadings $> 1 \text{ mg cm}^{-2}$. The loss of the catalyst material could, however, impact the performance of the next generation, low loaded anodes in PEWE ($\lesssim 0.5 \text{ mg Ir cm}^{-2}$) [4], and warrants further investigation.

4. Conclusion

PEWE cells were subjected to materials and operating conditions to promote mechanical deformation and dissolution of the anode catalyst

layer. Creep of the CCM into the PTL pores, and the subsequent compaction of the anode CL by the PTL particles caused fissures in the catalyst layer structure, disrupting its electronic and ionic pathways. As a result, the proton transport resistance had increased 3-fold for the mechanically stressed cell, explaining higher measured mass transport losses. Creep of the CCM had induced higher gas crossover, and as a result higher FRR in the case of the mechanically stressed cell, linking mechanical and chemical degradation mechanisms. Development of PTLs with a microporous interface to the CL would not only be beneficial for decreasing the ohmic losses through the reduction of contact resistances in a PEWE cell. A smooth PTL interface could prevent creep of the CCM and preserve the structure of CLs. Start-stop experiments (2.2 V/1.8 V – OCV) initially revealed a beneficial effect on the cell performance through the formation of active Ir-hydroxo species. More Ir was detected in the CCM cross-section of the cell operated at higher on-state potential, with both cells emitting similar amounts of Ir into the anodic water. Loss of Ir during start-stop operation did not lead to an increase of kinetic losses during 300 h.

Declaration of competing interest

The authors declare that they have no known competing financial interests or personal relationships that could have appeared to influence the work reported in this paper.

Acknowledgments

The authors thank the Swiss Federal Office of Energy (BFE), grant ELY-DEG SI/501198-01 for funding of the project. TJS thanks Innosuisse and the Swiss Competence Center for Energy Research (SCCER) Heat & Electricity Storage. Technical and scientific support from Thomas Gloor during ion chromatography measurements are gratefully acknowledged.

Appendix A. Supplementary data

Supplementary data to this article can be found online at <https://doi.org/10.1016/j.jpowsour.2020.227778>.

References

- [1] R. Winkler-Goldstein, A. Rastetter, *Green* 3 (2013) 69–78.
- [2] G. Gahleitner, *Int. J. Hydrogen Energy* 38 (2013) 2039–2061.
- [3] A. Buttler, H. Spliethoff, *Renew. Sustain. Energy Rev.* 82 (2018) 2440–2454.
- [4] U. Babic, M. Suermann, F.N. Büchi, L. Gubler, T.J. Schmidt, *J. Electrochem. Soc.* 164 (2017) F387–F399.
- [5] M. Carmo, D.L. Fritz, J. Mergel, D. Stolten, *Int. J. Hydrogen Energy* 38 (2013) 4901–4934.
- [6] L. Bertuccioli, A. Chan, D. Hart, F. Lehner, B. Madden, E. Standen, Study on Development of Water Electrolysis in the EU by E4tech Sàrl with Element Energy Ltd for the Fuel Cells and Hydrogen Joint Undertaking, 2014.
- [7] DOE Technical Targets for Hydrogen Production from Electrolysis, Office of Energy Efficiency & Renewable Energy, 2015 retrieved from, <http://energy.gov/eere/fuelcells/doe-technical-targets-hydrogen-production-electrolysis>. (Accessed 11 April 2018).
- [8] O. Schmidt, A. Gambhir, I. Staffell, A. Hawkes, J. Nelson, S. Few, *Int. J. Hydrogen Energy* 42 (2017) 30470–30492.
- [9] P. Lettenmeier, R. Wang, R. Abouatallah, B. Saruhan, O. Freitag, P. Gazdzicki, T. Morawietz, R. Hiesgen, A.S. Gago, K.A. Friedrich, *Sci. Rep.* 7 (2017), 44035, <https://doi.org/10.1038/srep44035>.
- [10] C. Rakousky, U. Reimer, K. Wippermann, M. Carmo, W. Lueke, D. Stolten, *J. Power Sources* 326 (2016) 120–128.
- [11] T. Schuler, R. De Bruycker, T.J. Schmidt, F.N. Büchi, *J. Electrochem. Soc.* 166 (2019) F270–F281.
- [12] S.H. Frensch, A.C. Olesen, S.S. Araya, S.K. Kær, *Electrochim. Acta* 263 (2018) 228–236.
- [13] U. Babic, T.J. Schmidt, L. Gubler, *J. Electrochem. Soc.* 165 (2018) J3016–J3018.
- [14] M. Suermann, T.J. Schmidt, F.N. Büchi, *Electrochim. Acta* 211 (2016) 989–997.
- [15] M. Suermann, K. Takanoashi, A. Lamibrac, T.J. Schmidt, F.N. Büchi, *J. Electrochem. Soc.* 164 (2017) F973–F980.
- [16] H. Ito, T. Maeda, A. Nakano, A. Kato, T. Yoshida, *Electrochim. Acta* 100 (2013) 242–248.
- [17] M. Bernt, A. Siebel, H. Gasteiger, *J. Electrochem. Soc.* 165 (2018) F305–F314.
- [18] D. Lebedev, M. Povia, K. Waltar, P.M. Abdala, I.E. Castelli, E. Fabbri, M.V. Blanco, A. Fedorov, C. Copéret, N. Marzari, T.J. Schmidt, *Chem. Mater.* 29 (2017) 5182–5191.
- [19] L.C. Seitz, C.F. Dickens, K. Nishio, Y. Hikita, J. Montoya, A. Doyle, C. Kirk, A. Vojvodic, H.Y. Hwang, J.K. Nørskov, T.F. Jaramillo, *Science* 353 (2016) 1011–1014.
- [20] H. Yu, N. Y. Wang, W. Willis, A. Poozhikunnath, L. Bonville, C. Capuano, K. Ayers, R. Maric, *Appl. Catal. B Environ.* 239 (2018) 133–146.
- [21] E. Fabbri, A. Habereeder, K. Waltar, R. Kötter, T.J. Schmidt, *Catal. Sci. Technol.* 4 (2014) 3800–3821.
- [22] E. Oakton, D. Lebedev, A. Fedorov, F. Krumeich, J. Tillier, O. Sereda, T.J. Schmidt, C. Coperet, *New J. Chem.* 40 (2016) 1834–1838.
- [23] E. Oakton, D. Lebedev, M. Povia, D.F. Abbott, E. Fabbri, A. Fedorov, M. Nachtegaal, C. Copéret, T.J. Schmidt, *ACS Catal.* 7 (2017) 2346–2352.
- [24] K.A. Lewinski, D.F.v.d. Vliet, S.M. Luopa, *ECS Trans.* 69 (2015) 893–917.
- [25] C. Rozain, E. Mayousse, N. Guillet, P. Millet, *Appl. Catal. B Environ.* 182 (2016) 153–160.
- [26] M. Bernt, H.A. Gasteiger, *J. Electrochem. Soc.* 163 (2016) F3179–F3189.
- [27] J. Mo, Z. Kang, S.T. Retterer, D.A. Cullen, T.J. Toops, J.B. Green, M.M. Mench, F.-Y. Zhang, *Sci. Adv.* 2 (2016), e1600690.
- [28] O. Kasian, S. Geiger, P. Stock, G. Polymeros, B. Breitbach, A. Savan, A. Ludwig, S. Cherevko, K.J.J. Mayrhofer, *J. Electrochem. Soc.* 163 (2016) F3099–F3104.
- [29] S. Cherevko, S. Geiger, O. Kasian, N. Kulyk, J.-P. Grote, A. Savan, B.R. Shrestha, S. Merzlikin, B. Breitbach, A. Ludwig, K.J.J. Mayrhofer, *Catal. Today* 262 (2016) 170–180.
- [30] O. Kasian, J.P. Grote, S. Geiger, S. Cherevko, K.J.J. Mayrhofer, *Angew. Chem. Int. Ed. Engl.* 57 (2018) 2488–2491.
- [31] S. Cherevko, T. Reier, A.R. Zeradjanin, Z. Pawolek, P. Strasser, K.J.J. Mayrhofer, *Electrochem. Commun.* 48 (2014) 81–85.
- [32] A. Weiß, A. Siebel, M. Bernt, T.-H. Shen, V. Tileli, H.A. Gasteiger, Impact of Intermittent Operation on Lifetime and Performance of a PEM Water Electrolyzer, vol. 166, 2019, pp. F487–F497, 8.
- [33] P. Lettenmeier, R. Wang, R. Abouatallah, S. Helmly, T. Morawietz, R. Hiesgen, S. Kolb, F. Burggraf, J. Kallo, A.S. Gago, K.A. Friedrich, *Electrochim. Acta* 210 (2016) 502–511.
- [34] D.F. Abbott, D. Lebedev, K. Waltar, M. Povia, M. Nachtegaal, E. Fabbri, C. Copéret, T.J. Schmidt, *Chem. Mater.* 28 (2016) 6591–6604.
- [35] U. Babic, E. Nilsson, A. Pătru, T.J. Schmidt, L. Gubler, *J. Electrochem. Soc.* 166 (2019) F214–F220.
- [36] H. Ito, T. Maeda, A. Nakano, A. Kato, T. Yoshida, *Electrochim. Acta* 100 (2013) 242–248.
- [37] P. Trinke, B. Bensmann, R. Hanke-Rauschenbach, *Int. J. Hydrogen Energy* 42 (2017) 14355–14366.
- [38] L. Gubler, S.M. Dockheer, W.H. Koppenol, *J. Electrochem. Soc.* 158 (2011) B755–B769.
- [39] M. Inaba, T. Kinumoto, M. Kiriake, R. Umebayashi, A. Tasaka, Z. Ogumi, *Electrochim. Acta* 51 (2006) 5746–5753.
- [40] R. Singh, P.C. Sui, K.H. Wong, E. Kjeang, S. Knights, N. Djilali, *J. Electrochem. Soc.* 165 (2018) F3328–F3336.
- [41] H. Liu, F.D. Coms, J. Zhang, H.A. Gasteiger, A.B. LaConti, Chemical degradation: correlations between electrolyzer and fuel cell findings, in: F.N. Büchi, M. Inaba, T. J. Schmidt (Eds.), *Polymer Electrolyte Fuel Cell Durability*, Springer-Verlag New York, New York, USA, 2009, pp. 71–116.
- [42] M. Takasaki, Y. Nakagawa, Y. Sakiyama, K. Tanabe, K. Ookubo, N. Sato, T. Minamide, H. Nakayama, M. Hori, *ECS Trans.* 17 (2009) 439–447.
- [43] P. Jovanović, N. Hodnik, F. Ruiz-Zepeda, I. Arçon, B. Jozinović, M. Zorko, M. Bele, M. Šala, V.S. Šelih, S. Hočevar, M. Gaberšček, *J. Am. Chem. Soc.* 139 (2017) 12837–12846.
- [44] C. Liu, M. Carmo, G. Bender, A. Everwand, T. Lickert, J.L. Young, T. Smolinka, D. Stolten, W. Lehnert, *Electrochem. Commun.* 97 (2018) 96–99.
- [45] R. Woods, *J. Electroanal. Chem. Interfacial Electrochem.* 49 (1974) 217–226.